

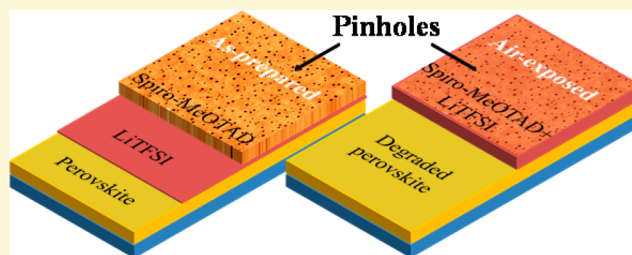
# Air-Exposure Induced Dopant Redistribution and Energy Level Shifts in Spin-Coated Spiro-MeOTAD Films

Zafer Hawash, Luis K. Ono, Sonia R. Raga, Michael V. Lee, and Yabing Qi\*

Energy Materials and Surface Sciences Unit (EMSS), Okinawa Institute of Science and Technology Graduate University (OIST), 1919-1 Tancha, Onna-son, Okinawa 904-0495 Japan

## Supporting Information

**ABSTRACT:** Doping properties of 2,2',7,7'-tetrakis(*N,N*-di-*p*-methoxyphenylamine)-9,9'-spirobifluorene (spiro-MeOTAD) hole transport layer are investigated by X-ray photoelectron spectroscopy, ultraviolet photoelectron spectroscopy, and atomic force microscopy under air exposure. XPS results reveal that 3 h exposure of Li-bis(trifluoromethanesulfonyl)-imide (LiTFSI) doped spiro-MeOTAD to air results in the migration of LiTFSI from the bottom to the top across the spiro-MeOTAD film. AFM images reveal the presence of pinholes with an average diameter of  $\sim 135$  nm and a density of  $\sim 3.72$  holes/ $\mu\text{m}^2$ . In addition, cross-sectional scanning electron microscope images reveal that these pinholes form channels across the doped spiro-MeOTAD film. Optical microscopy and Fourier transform infrared microscopy images confirm the presence of large pinholes with diameters in the range of 1–20  $\mu\text{m}$  and a density of  $\sim 289$  holes/ $\text{mm}^2$  as well. The presence of pinholes may play a major role in the migration processes of the LiTFSI within the spiro-MeOTAD film as well as on the degradation processes of solar cells. This is further confirmed by the rapid decreasing efficiency of perovskite solar cells with solution prepared doped spiro-MeOTAD layers when exposed to air.



## 1. INTRODUCTION

Solar energy-to-electricity power conversion efficiencies (PCEs) of solid-state dye-sensitized solar cells (DSSCs) have rapidly progressed in the past few years. One of the leading improvements of the solid-state DSSC compared to the previous DSSC was the replacement of the liquid electrolyte with solid organic hole transport layers (HTLs).<sup>1,2</sup> The replacement of the electrolyte with 2,2',7,7'-tetrakis(*N,N*-di-*p*-methoxyphenylamine)-9,9'-spirobifluorene (spiro-MeOTAD) HTL not only solved the problem of leakage and sealing issues but also culminated as one of the most important HTLs for solid-state DSSCs as well as for perovskite-based solar cells.<sup>3–5</sup> Spiro-MeOTAD is a widely used HTL in current high-performance solid-state cells, mostly due to its high stability (glass-transition temperature  $T_g = 121$  °C), high solubility, and amorphous nature.<sup>6–9</sup> Material infiltration into the mesoporous  $\text{TiO}_2$  layers of up to a few micrometers has been reported.<sup>8</sup> The first report employing spiro-MeOTAD mixed with  $\text{Li}(\text{CF}_3\text{SO}_2)_2\text{N}$  (Li-bis(trifluoromethanesulfonyl)-imide, LiTFSI) and  $\text{N}(\text{PhBr})_3\text{-SbCl}_6$  (tris(4-bromophenyl)-ammonium hexachloroantimonate) as additives had a low PCE of  $\sim 0.74\%$ .<sup>2</sup> Interfacial charge recombination processes taking place between dye/ $\text{TiO}_2$ , HTL/ $\text{TiO}_2$ , and HTL/dye were pin-pointed as the origin for the low efficiencies.<sup>2,10</sup> Thus, the composition of the HTL was further modified blending 4-*tert*-butylpyridine (*t*-BP) and LiTFSI, which reduced charge recombination under optimized conditions. The addition of *t*-BP showed 100% improvement in the open-circuit voltage

( $V_{oc}$ ) and LiTFSI improved the short-circuit current ( $J_{sc}$ ) and hence resulted in overall enhancement of  $\sim 2.56\%$  in PCE.<sup>10</sup> Such optimized doped spiro-MeOTAD was used as a standard HTL for the solid-state DSSCs together with different organic dyes.<sup>11–13</sup> The highest certified efficiency of 6.08% has been reported using the C220 dye molecules.<sup>14</sup> More recently, when combined with an organometallic perovskite absorber, the same optimized HTL resulted in  $\sim 9\%$  PCE.<sup>3,15</sup> Currently, the same recipe that includes the *t*-BP and LiTFSI doped spiro-MeOTAD as HTL prevails in perovskite-based solar cells and reported to achieve high efficiencies  $> 15\%$ .<sup>16–18</sup>

Spiro-MeOTAD in its pristine form suffers from the low hole mobility and conductivity.<sup>19–21</sup> Thus, inclusion of a dopant (e.g., LiTFSI) helps not only generate additional charge carriers but also tune the electronic properties such as the energy level alignment at the interfaces.<sup>22–24</sup> The doping of spiro-MeOTAD is generally associated with the oxidation reaction, and efforts have been made to find suitable dopants that effectively dope spiro-MeOTAD.<sup>22–27</sup> In the presence of LiTFSI dopant, spiro-MeOTAD is not readily oxidized in the presence of light or in the dark and the oxidation reaction is only promoted upon air exposure.<sup>19,28,29</sup> In contrast to organic solar cells, where air exposure leads to degradation of devices, air exposure is necessary during device fabrication in order to obtain a working

Received: October 31, 2014

Revised: December 26, 2014

Published: December 29, 2014

perovskite cell.<sup>28,30</sup> On the other hand, a fundamental understanding remains elusive regarding the processes taking place when the LiTFSI doped spiro-MeOTAD film is exposed to air. In this work, we studied the electronic structure and the chemical composition of the doped spiro-MeOTAD and its interactions with air exposure. Comparisons are made to undoped spiro-MeOTAD and spiro-MeOTAD films with only *t*-BP. Segregation of LiTFSI to the top surface evolves as a function of air exposure time. Microscopy techniques revealed the presence of pinholes in those films, which is a possible factor to facilitate the diffusion of the dopant upon air exposure as well as on the degradation processes of the active materials (e.g., perovskite). Our combined techniques of spectroscopy and microscopy presented in this work are expected to help the screening process of finding alternative suitable HTL materials with pinhole free films, high stability upon air exposure, and good energy level alignments.

## 2. EXPERIMENTAL SECTION

Doped spiro-MeOTAD solution (Figure 1) was prepared according to the standard literature procedure reported elsewhere.<sup>10</sup> Briefly, spiro-

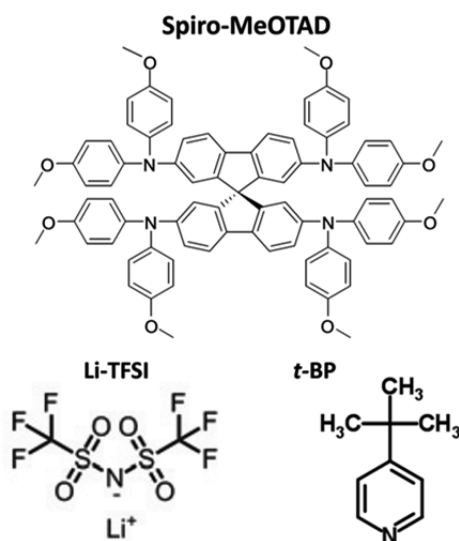


**Figure 1.** Molecular structures of LiTFSI, *t*-BP, and spiro-MeOTAD composing the doped spiro-MeOTAD hole transport material.

MeOTAD (SHT-263, Merck KGaA) was dissolved in chlorobenzene and mixed with 4-*tert*-butylpyridine (*t*-BP, Sigma) and acetonitrile (52 mg/100  $\mu$ L) dissolved Li-bis(trifluoromethanesulfonyl)-imide (LiTFSI, Sigma). The final solution had concentrations of 56.4 mM of spiro-MeOTAD, 187.9 mM of LiTFSI, and 30.46 mM of *t*-BP. Thus, the corresponding molar ratios of spiro-MeOTAD:LiTFSI:*t*-BP were 1:3.33:0.54 based on the nominal concentrations. For photoemission spectroscopy studies, thin films of doped spiro-MeOTAD were prepared by spin-coating in the nitrogen glovebox for 60 s at a speed of 2000 rpm. Spin-coating was performed on thermally evaporated 120 nm of Au (Denton Vacuum Evaporator, Model DV-502 V) on heavily doped Si substrates with a thin native SiO<sub>2</sub> layer (SAMCO Inc., 0.013  $\Omega$ -cm). The final thickness of doped spiro-MeOTAD films was approximately 240 nm, determined by a profilometer (Dektak stylus profiler, Bruker).

Perovskite solar cells with doped spiro-MeOTAD were prepared on glass substrates coated with F-doped SnO<sub>2</sub> (FTO, Pilkington 7  $\Omega$  sq<sup>-1</sup>). FTO was etched with Zn powder and HCl and subsequently cleaned by brushing with detergent, rinsing with Milli-Q water, and sonicating with 2-propanol. An 80 nm thick TiO<sub>2</sub> compact layer was deposited by spray pyrolysis using a mixture of Ti (IV) isopropoxide,

acetylacetone, and anhydrous ethanol with the weight ratio of 3:3:2. Perovskite film precursor was deposited by spin-coating at 2000 rpm for 45 s from a mixture of methylammonium iodide (MAI) and PbCl<sub>2</sub> with the weight ratio of 2.5:1 in dimethylformamide. Perovskite crystal growth was performed by annealing the films on a hot plate at 110  $^{\circ}$ C for 45 min in a N<sub>2</sub> glovebox with O<sub>2</sub> and H<sub>2</sub>O levels below 0.1 ppm. HTL consisting of LiTFSI and *t*-BP doped spiro-MeOTAD solution described above was deposited by spin-coating at 2000 rpm for 60 s. Finally, top gold contacts (70 nm) were deposited by thermal evaporation in a vacuum chamber.

The electronic properties of the doped spiro-MeOTAD films were characterized by ultraviolet photoelectron spectroscopy (UPS, Kratos AXIS ULTRA HAS, He-I $\alpha$  = 21.22 eV), and the data analysis was performed in Origin Pro 9. The analysis of UPS was complemented by X-ray photoemission spectroscopy (XPS, Kratos AXIS ULTRA HAS, monochromated Al K $\alpha$  = 1486.6 eV). XPS was performed to monitor the chemical states of the as-prepared spiro-MeOTAD, vacuum stored, air- and nitrogen-exposed films. The binding energy (BE) for UPS and XPS was calibrated by measuring the Fermi edge ( $E_F$  = 0 eV) and Au-4f<sub>7/2</sub> (84.0 eV) on a clean Au surface. The estimated energy resolutions of UPS and XPS were 0.14 and 0.7 eV, respectively. Analysis of the XPS data was performed in CasaXPS 2.3.16 software. UV and X-ray induced sample damage was monitored by taking five consecutive spectra and comparing those spectra. The time acquisition for each scan varied from 10 to 20 s depending on the core level regions. The five scans were averaged to a single spectrum if no changes were observed among these five spectra. Individual spin-coated films of spiro-MeOTAD, LiTFSI, and *t*-BP were examined under UV and X-ray radiation. A small peak corresponding to the LiF compound was observed at higher BE in the F-1s region (~685 eV) as well as TFSI at lower BE (~402 eV) in the N-1s region, both of which were a result of the decomposition of LiTFSI (Figure S3, Supporting Information) upon UV and X-ray exposures.<sup>31</sup> Thus, special care was taken to minimize the UV and X-ray exposure time when acquiring UPS/XPS on doped spiro-MeOTAD films. No X-ray and UV induced damages were observed on spiro-MeOTAD molecules. The XPS detection of spin-coated or drop-casted *t*-BP compound on Au film was below the sensitivity of the system when the samples were loaded into the vacuum chamber. Because of the high vapor pressure of *t*-BP, it was not possible to obtain reference UPS and XPS spectra for *t*-BP spin-coated on Au. For the investigation of the influence of *t*-BP on spiro-MeOTAD, *t*-BP solution with 10 times higher concentration was mixed with spiro-MeOTAD and films were prepared by spin-coating.

The morphological characterization of the films was performed *ex situ* by AFM in tapping-mode (MFP-3D series, Asylum Research), and the quantitative analysis was conducted using WsXM 5.0 software. The cross-sectional scanning electron microscope (SEM) images were taken at 1.5 kV with a through the lens detector (TLD) for detecting secondary electrons (FEI, Helios NanoLab 650). Multiple samples were prepared for the cross-sectional SEM by cleaving manually the doped spiro-MeOTAD deposited on the Au(120 nm)/SiO<sub>2</sub>(native oxide)/Si substrate by using a diamond scribe from the backside of the sample. Air exposure experiments were performed on doped spiro-MeOTAD films exposed to the laboratory air in the dark (samples stored in a stainless steel container). The measured laboratory humidity and temperature were approximately 37% and 24  $^{\circ}$ C, respectively. Controlled nitrogen exposure experiments were conducted in the loadlock of the XPS system (nitrogen gas pressure = 1 atm). Time evolution of the films' chemical states was also monitored by storing the samples in vacuum ( $2 \times 10^{-9}$  Torr) for the same period of times used for the different gas exposures to rule out any measurement-induced artifacts (such as UV and X-ray radiation). No indication of radiation induced changes (e.g., dopant segregation, spiro-MeOTAD oxidation, and fragmentation of different chemical compounds) was observed by UPS and XPS on the doped spiro-MeOTAD films with constant halogen light (strong intensity in the visible range) illumination.

Molecular information was investigated with Fourier transform infrared (FTIR) microscopy, using an Agilent Cary 620 FTIR microscope coupled to a Cary 670 mid-IR spectrometer. Spectral

images were obtained using normal and high magnification optics using high NA reflective lenses. The incident IR beam passed through the spiro-MeOTAD films, reflected off the gold, and passed a second time through the films using transfection mode. Peaks from spiro-MeOTAD, *t*-BP, and LiTFSI were observed. The resolution of the images was on the order of a few microns, so only the larger 1–20  $\mu\text{m}$  holes could be observed by FTIR microscopy.

Solar cell efficiencies were extracted from current–voltage ( $I$ – $V$ ) curves measured by a source meter (Keithley, 2420) under 1 sun illumination (AM 1.5G, 100  $\text{mW cm}^{-2}$ ) using a solar simulator (Newport, Oriel Sol1A). For the stability tests, the “air-exposed” samples were stored in a Petri dish in laboratory air wrapped in aluminum foil and the “vacuum-exposed” samples were stored in a vacuum chamber with the pressure kept at  $10^{-7}$  Torr.

### 3. RESULTS AND DISCUSSION

Changes in the electronic properties of the as-prepared doped spiro-MeOTAD film after air exposure were probed by UPS with a He– $I\alpha$  source (Figure 2). The leading edge of the

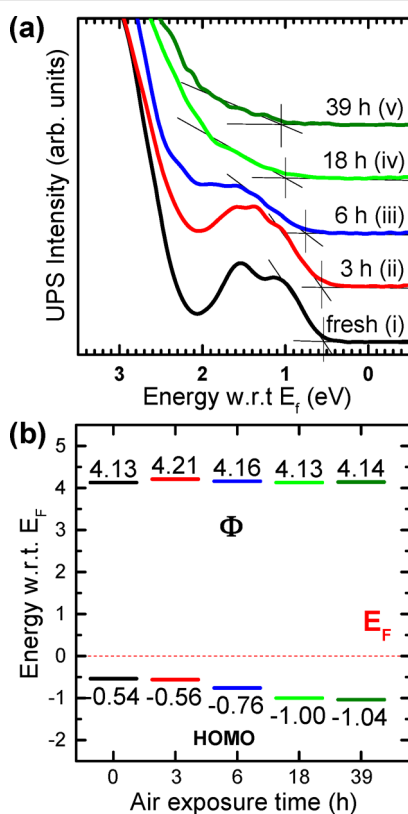


**Figure 2.** (a) UPS spectra (He– $I\alpha$  = 21.22 eV) corresponding to the HOMO region of the as-prepared doped spiro-MeOTAD film (i) and the same sample when exposed to air for 3 h (ii), 6 h (iii), 18 h (iv), and 39 h (v). (b) Corresponding schematic energy diagram of doped spiro-MeOTAD film.

highest occupied molecular orbital (HOMO) with respect to the Fermi level (w.r.t.  $E_F$ ) for the as-prepared doped spiro-MeOTAD films was at  $-0.54$  eV (Figure 2a, spectrum i). After the initial 3 h air exposure, the HOMO level of the doped spiro-MeOTAD film showed a slight shift toward high BEs, settling at  $-0.56$  eV (Figure 2a, spectrum ii). An additional 3 h of exposure (Figure 2a, spectrum iii) induced a large shift, bringing the HOMO leading edge to  $-0.76$  eV, followed by an overall decrease in the intensity of the HOMO features. With a total of 18 or 39 h of air exposure (Figure 2a, spectra iv and v),

the HOMO further shifted with the leading edges at  $-1.00$  and  $-1.04$  eV, respectively. An almost complete disappearance of the HOMO features was observed after the 18 h air exposure. Nevertheless, the high sensitivity of our UPS system made it still possible to extract unambiguously the leading edge position that was distinguishable above the background signal. As seen from Figure 2a, a substantial HOMO level shift occurred during the first 6 h and saturation was reached after 18 h. Figure 2b displays the schematic energy diagram showing the time evolution of the work function ( $\Phi$ ) and HOMO leading edge values w.r.t.  $E_F$  on the doped spiro-MeOTAD films with air exposure. The  $\Phi$  values were determined from the cutoff edge observed in the high BE side of the UPS spectra (Figure S1a, Supporting Information). The extracted  $\Phi$  values were constant over the entire air exposure time in this experiment ( $\Phi = 4.15 \pm 0.03$  eV). The ionization energy (IE) was calculated to be 4.67 eV for the as-prepared doped spiro-MeOTAD film, which is  $\sim 0.3$  eV lower than the IE measured on the pristine spiro-MeOTAD film prepared by vacuum evaporation<sup>21</sup> and  $\sim 0.1$  eV lower than the pristine spiro-MeOTAD film prepared by solution processing (Figure S1b). The observed differences are possibly due to the different preparation methods used in these studies. Interestingly, the IE was observed to increase as a function of the air exposure time, from the initial value of 4.67 eV for the as-prepared film to a saturation value of  $\sim 5.1$  eV after 18 h air exposure. At the same time, as will be discussed later in the XPS section, the as-prepared LiTFSI doped spiro-MeOTAD shows a small amount of LiTFSI at the top surface. This indicates that a strong electronic interaction between spiro-MeOTAD molecules and LiTFSI prevails within the film upon air exposure. Two factors may contribute to the observed IE changes: (1) chemical changes of the spiro-MeOTAD induced by dopants or air exposure contamination (interaction induced by atmospheric aerosols),<sup>32</sup> and (2) the diffusion of dopants populating at the topmost surface.

After each UPS measurement, XPS was recorded to monitor the chemical states of the doped spiro-MeOTAD films. Figure 3 shows the XPS C-1s (a), Li-1s (b), and F-1s (c) core levels of the doped spiro-MeOTAD film for the as-prepared sample (i) and the same sample after the different air exposure periods: after 3 h (ii), 6 h (iii), 18 h (iv), and 39 h (v). The XPS O-1s, S-2p, and N-1s core levels were also measured and are displayed in Figure S2 (Supporting Information). The as-prepared doped spiro-MeOTAD film shows the overall C-1s spectrum shape that is similar to the pristine spiro-MeOTAD.<sup>21,22,33,34</sup> A small F-1s signal ( $\sim 2.2\%$ ) corresponding to LiTFSI (Figures 3b,c and 4) was observed, meaning that a diluted LiTFSI concentration is present at the top surface on the as-prepared film. Because doped spiro-MeOTAD films are composed of three chemical compounds (Figure 1), the overlapping of C–H, C–C, and C–N signals from spiro-MeOTAD and *t*-BP molecules is unavoidable. Thus, curve fitting analysis in the C-1s region is challenging. XPS measurements on spiro-MeOTAD mixed with *t*-BP film compared with pristine spiro-MeOTAD film did not show any difference (Figure S4, Supporting Information).

Although spectra for the *t*-BP could not be measured by XPS, the presence of *t*-BP was confirmed by FTIR. Undoped and doped spiro-MeOTAD films were measured by FTIR. Additional peaks were observed in the doped films that correlate to peaks from *t*-BP in reference spectra<sup>35</sup> and LiTFSI spectra in the literature.<sup>19,36</sup> A further detailed description is given in the Supporting Information.



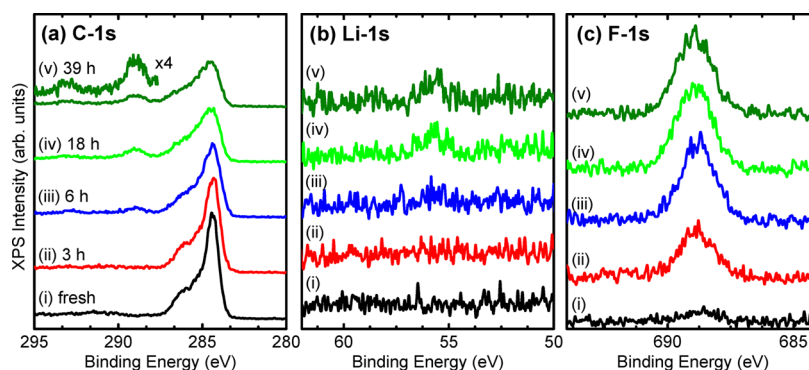


**Figure 3.** XPS spectra ( $Al-K\alpha = 1486.6$  eV) corresponding to (a) C-1s, (b) Li-1s, and (c) F-1s core levels of the as-prepared doped spiro-MeOTAD films (i) and subsequent after 3 h (ii), 6 h (iii), 18 h (iv), and 39 h air exposure (v).

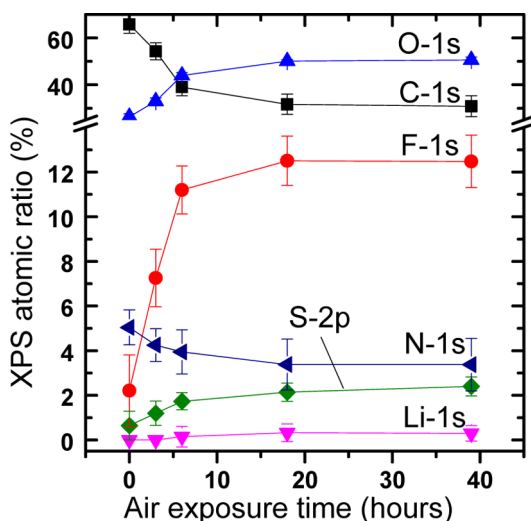


**Figure 4.** XPS atomic ratio variations for C-1s, O-1s, S-2p, N-1s, Li-1s, and F-1s when doped spiro-MeOTAD is exposed to air.

In contrast, the LiTFSI compound was observed to show the characteristic signatures in XPS<sup>31</sup> such as Li and high oxidative-shifted carbon ( $-CF_3$ ) (Figure 3b,c), which enables unambiguous detection. The C-1s peak maximum of the as-prepared LiTFSI doped spiro-MeOTAD was located at a BE of  $\sim 284.5$  eV. For comparison, the typical C-1s peak maximum BE value reported for the undoped spiro-MeOTAD is  $\sim 285.1$ – $285.4$  eV.<sup>21,22,33,34</sup> Thus, XPS also confirmed that the dopants induced a Fermi level shift toward the HOMO by  $\sim 0.6$ – $0.9$  eV, consistent with the p-type doping previously discussed for the UPS analysis (Figure 2). After 3 h air exposure, a new peak appeared at  $\sim 688.6$  eV that was attributed to F-1s of the  $-CF_3$  groups in TFSI.<sup>31</sup> Such an observation confirms the redistribution of the LiTFSI within the doped spiro-MeOTAD film to reach the top surface driven by the air exposure. Thus, the as-prepared films seem to have phase segregated concentrations of spiro-MeOTAD and LiTFSI within the film where high concentrations of LiTFSI were initially located at the bottom region of the film (i.e., the region close to the Au substrate). Upon air exposure, the LiTFSI diffusion starts to take place, segregating to the top surface of the film. Because of the high atomic sensitivity factor (ASF) of the F-1s signal ( $ASF = 4.43$ ) compared to the Li-1s ( $ASF = 0.06$ ) and C-1s ( $ASF = 1$ ),<sup>37</sup> the changes in the C-1s and Li-1s regions are minimal (Figure 3a,b, spectrum ii). Clear signatures of the LiTFSI were only observed after 18 h (Figure 3) with the Li-1s peak

centered at  $\sim 56$  eV, C-1s at 293 eV, and S-2p at  $\sim 170$  eV (Figure S2b).<sup>31,34,38</sup> The O-1s and N-1s regions (Figure S2) corroborate as well with the picture of the segregation of LiTFSI to the top surface. In the S-2p region; the appearance of doublet peaks ( $2p_{3/2} = 169.3$  eV and  $2p_{1/2} = 170.5$  eV) due to spin–orbit splitting was observed after the initial 3 h air exposure.<sup>38</sup> The S-2p photoemission was assigned to the  $-SO_2-$  group of the LiTFSI.<sup>38</sup> In the O-1s region, the as-prepared film showed two components, one centered at  $\sim 532$  eV and the other at  $\sim 533$  eV. The O-1s peak at  $\sim 532$  eV belongs to LiTFSI and was detected in the as-prepared film due to the high ASF value of O-1s ( $ASF = 2.93$ ). After 3 h air exposure, the lower BE shoulder ( $\sim 532$  eV) was observed to increase in intensity, which can be assigned to the LiTFSI.<sup>38</sup> The other high BE component was assigned to the  $C_a-O-C$  group (where  $C_a$  corresponds to the aromatic C) in spiro-MeOTAD.<sup>21</sup> In the N-1s core level (Figure S2c), a gradual broadening of the peak with increasing air exposure time was observed. Two components were deconvoluted with one at  $\sim 399.5$  eV and the other at  $\sim 400$  eV, which can be assigned to the C–N group in spiro-MeOTAD and imide group in LiTFSI, respectively.<sup>21,38</sup> XPS Li-1s and F-1s spectra measured on an as-prepared pure LiTFSI film (Figure S3) show the peak position and overall shape similar to the doped spiro-MeOTAD film case. Thus, it is expected that the majority of the LiTFSI molecules were found in their intact form; i.e., dissociation of Li from TFSI<sup>39</sup> was negligible (if any) in our experiments.

Additional secondary processes were observed from our XPS analysis induced by air exposure. For example, an additional peak in C-1s centered at  $\sim 289$  eV was observed after 6 h air exposure (Figure 3a, spectrum iii), which could be associated with air exposure contamination such as aerosols.<sup>32</sup> At the moment, it is difficult to assign the observed peak. A similar peak was reported by Schölin et al.<sup>34,40–42</sup> and was assigned as the oxidized form of spiro-MeOTAD. In addition, the C-1s peak maximum at 284.4 eV corresponding to C–H carbon in spiro-MeOTAD<sup>21,22</sup> decreases substantially in intensity while in the BE range between  $\sim 285$  and 287 eV (corresponding to carbon from C–C, C–N, and C–O in spiro-MeOTAD) is less affected by the air exposure. As described in the Experimental Section, caution was taken to minimize the X-ray time exposure when acquiring UPS and XPS on doped spiro-MeOTAD films. Thus, the aforementioned secondary processes observed in doped spiro-MeOTAD (appearance of  $\sim 289$  eV peak and significant decay of the 284.4 eV peak in C-1s) are expected to be induced mainly from the air exposure step. In addition, we did not observe similar behavior in the XPS core levels or

HOMO leading edges of the doped spiro-MeOTAD films when samples were kept in vacuum or in a dry  $N_2$  environment (Figures S5–S8, Supporting Information).

The effect of air exposure over time on the doped spiro-MeOTAD film surface induced by the presence of gas molecules was monitored by the quantitative analysis of the XPS data (Figure 4). XPS relative atomic ratios of O-1s, N-1s, C-1s, F-1s, S-2p, and Li-1s were calculated by summing the integrated peak area values of all species in each region, followed by normalization on the basis of the respective ASF values. Each spiro-MeOTAD molecule is composed of 81 C atoms, 8 O atoms, and 4 N atoms (Figure 1). The *t*-BP molecules, as discussed in the XPS section, facilitates the solubility of the LiTFSI and will mostly desorb from the surface when transferred to vacuum.<sup>28</sup> In the case of the LiTFSI dopant, each molecule is composed of 2 C atoms, 6 F atoms, 1 Li atom, 1 N atom, 4 O atoms, and 2 S atoms (Figure 1). A clear increase in O-1s, F-1s, S-2p, and Li-1s atomic ratios was observed as air exposure time increases, meaning that a dynamic process of redistribution of the LiTFSI to the top surface takes place. On the other hand, the atomic ratios of C-1s and N-1s decrease substantially. If LiTFSI molecules segregate to the top surface in their intact form, then the atomic ratios of C-1s and N-1s from the dopant would be expected to increase, but if one LiTFSI molecule displaces a spiro-MeOTAD molecule, then the overall atomic ratios of C-1s should decrease. On the other hand, it is difficult to expect the overall ratio of N-1s without knowing each component concentration on the surface. Therefore, the secondary processes cannot be neglected here. As described above, the photoemission spectroscopy analysis upon air exposure was complex due to the different gas molecules present in ambient air ( $N_2$ ,  $O_2$ ,  $H_2O$ ,  $CO_2$ , etc.). Furthermore, special care in the XPS analysis has to be taken, considering the effects of adventitious carbon compounds typically assigned as contamination in the literature.<sup>40–42</sup> To pinpoint the gas element(s) responsible for the segregation of the LiTFSI and unravel the observed secondary processes, further systematic studies to expose the doped spiro-MeOTAD films under controlled environments of  $O_2$ ,  $H_2O + N_2$ , and synthetic air are currently under further investigation.

Figure 5 shows AFM topography images of the as-prepared doped spiro-MeOTAD film (a) and after 24 h air exposure (b). As we can see from Figure 5, a large density of pinholes of  $3.72 \text{ holes}/\mu\text{m}^2$  was detected in the as-prepared films as well as in the air-exposed films. Based on the quantitative analysis of those images, the integrated area of all pinholes corresponds to about 6% of the total surface area with average diameters of 135 nm (Figure S9, Supporting Information). Similar holes were also detected when spiro-MeOTAD films were spin-coated on different substrates, including the ones precoated with perovskite films, suggesting the universal presence of these pinholes in spiro-MeOTAD films prepared by spin-coating. In addition, optical microscopy images of doped spiro-MeOTAD on a glass substrate showed large pinholes with diameters in the range of 1–20  $\mu\text{m}$  and a density of  $\sim 289 \text{ holes}/\text{mm}^2$ , which was extracted from  $2 \times 2 \text{ mm}^2$  area measurements (Figure S10, Supporting Information). FTIR under high magnification can also image these micron-scale holes and provides additional confirmation (Figure S11, Supporting Information). The existence of pinholes is reported to lead to shorts between the different layers in the organic devices,<sup>43</sup> and solutions have been sought in achieving robust devices.<sup>43–45</sup> These pinholes in

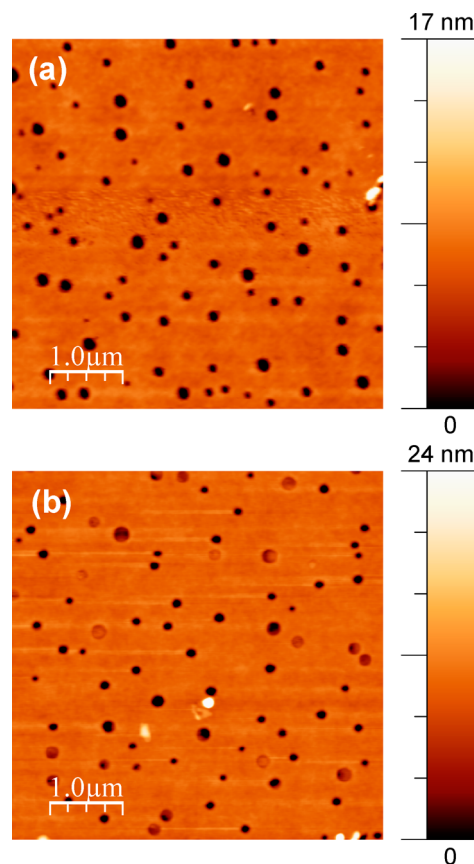


**Figure 5.** Tapping-mode AFM topography images of as-prepared doped spiro-MeOTAD, and after 24 h air exposure.

spiro-MeOTAD are also likely the cause for the very short lifetime commonly observed for perovskite solar cells that use spin-coated spiro-MeOTAD films as HTM. The effects can be possibly two-fold: (1) pinholes facilitate moisture migration through spiro-MeOTAD to reach perovskite layer and hence causing the degradation; (2) pinholes facilitate component elements from perovskite (e.g., iodine) to migrate to the top surface and degrade perovskite (decomposition). On the basis of such observations, to increase the lifetime of perovskite solar cells, it is necessary to optimize the preparation procedure of solution processed doped spiro-MeOTAD to avoid pinhole formation, e.g., by using different solvents, mixing with an additive, adding a top capping layer, etc.

To further provide insights on the morphology of those pinholes, cross-sectional SEM images were taken on multiple doped spiro-MeOTAD film samples (Figure 6). On the basis of the high magnification SEM image presented in Figure 6a, pinholes are observed to form channels across the film ( $\sim 240 \text{ nm}$  depth). The overall top surface image on the spiro-MeOTAD film reveals the high density of holes corroborating the AFM images (Figure 5) previously shown. As described in the Experimental Section, samples were prepared by cleaving the doped spiro-MeOTAD(240 nm)/Au(120 nm)/ $SiO_2$ (native oxide)/Si substrate by using a diamond scribe from the backside of the sample. This mechanical cleavage procedure was observed to tear apart the soft gold film together with the doped spiro-MeOTAD film, leaving a portion of the underneath substrate exposed. In addition, the gold film appears delaminated from the underneath substrate and at the edges of

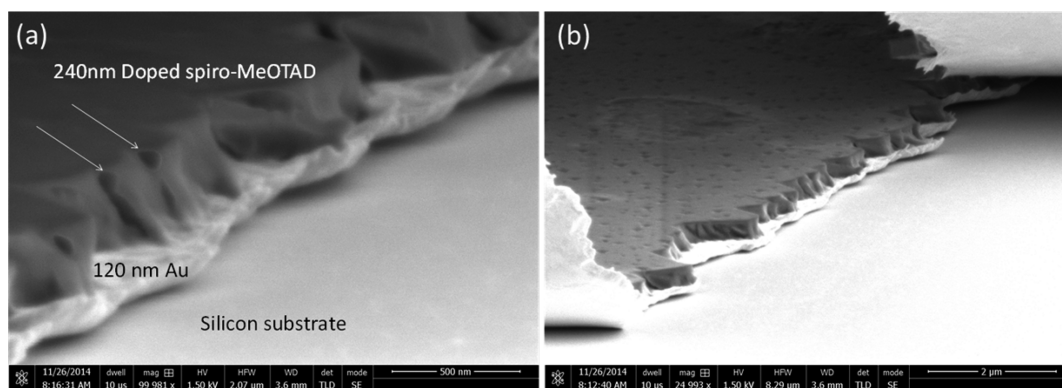


**Figure 6.** Cross-sectional SEM of doped spiro-MeOTAD film on Au: (a) pinholes form channels across the doped spiro-MeOTAD film indicated with arrows in high magnification image, and (b) the pinholes observed from the top surface of the film and from the cross section.

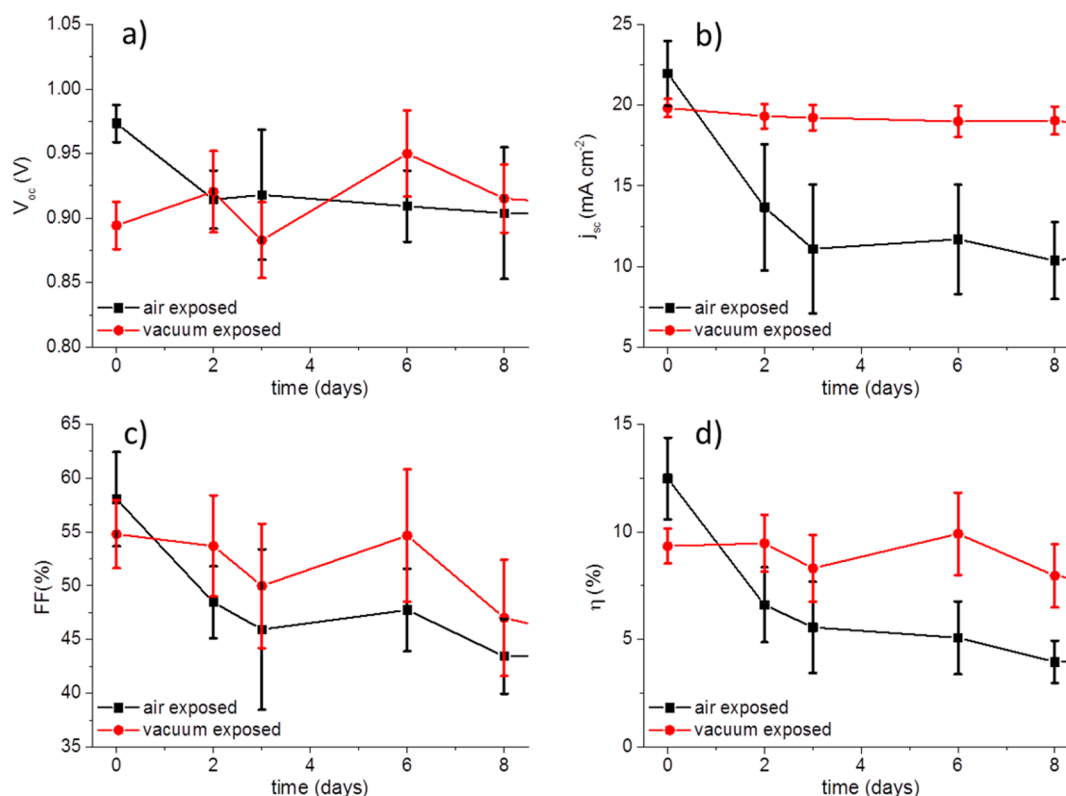


**Figure 7.** Evolution of the photovoltaic parameters with time: open-circuit voltage (a), short-circuit current density (b), fill factor (c), and power conversion efficiency (d). The points represent the average values from 6 samples with the corresponding standard deviation.

the image in Figure 6a,b, respectively, because the adhesion of the evaporated gold on silicon dioxide is very poor.

To further confirm the effect of the pinholes in conjunction with air exposure effects, we examined the time-dependent performance of perovskite solar cells employing spin-coated doped spiro-MeOTAD as HTL by exposing them to ambient conditions as well as to vacuum (as reference). Figure 7 shows the time evolution of two batches of doped spiro-MeOTAD based solar cells that were exposed in air and vacuum for 8 days. A progressive decrease of all the photovoltaic parameters were observed over time under air exposure, which was translated to a decrease of efficiency of 68% after 8 days. This degradation is remarkably faster within the first 2 days of air storage. On the other hand, when the solar cells were stored in vacuum for 8 days, the photocurrent remained almost the same, while photovoltage was slightly enhanced and fill factor decreased,

which overall resulted in an efficiency decrease of approximately 14%. The large decrease of  $J_{sc}$  was observed for the air-exposed solar cells, which is possibly related to the perovskite degradation induced by moisture.<sup>46,47</sup> This implies that water molecules diffuse through the spin-coated spiro-MeOTAD layer to reach the perovskite film and most likely this process is accelerated by the presence of pinholes.

#### 4. CONCLUSION

In summary, our XPS study reveals that (1) freshly prepared spiro-MeOTAD shows a very low concentration of LiTFSI dopants at the top surface and (2) air exposure causes some characteristic elements (e.g., F, S, and Li) belonging to LiTFSI to migrate to the top surface. This migration across the bulk film seems to be facilitated by the two types of pinholes with



different sizes, the presence of which is confirmed by AFM, SEM, and optical microscopy. The small-sized pinholes are partially filled up upon air exposure. The presence of pinholes may strongly affect the stability of the perovskite based solar cells using spin-coated spiro-MeOTAD as HTL. Therefore, it is necessary to optimize the preparation method for spin-coated doped spiro-MeOTAD.

## ■ ASSOCIATED CONTENT

### ● Supporting Information

UPS and XPS spectra on undoped spiro-MeOTAD films, spiro-MeOTAD + *t*-BP films, LiTFSI films, doped spiro-MeOTAD films stored in vacuum, and doped spiro-MeOTAD films stored in N<sub>2</sub>; AFM images analysis and optical microscopy image of doped spiro-MeOTAD; and FTIR microscopy on undoped and doped spiro-MeOTAD films. This material is available free of charge via the Internet at <http://pubs.acs.org>.

## ■ AUTHOR INFORMATION

### Corresponding Author

\*E-mail: Yabing.Qi@oist.jp (Y.B.Q.).

### Notes

The authors declare no competing financial interest.

## ■ ACKNOWLEDGMENTS

This work was supported by funding from the Okinawa Institute of Science and Technology Graduate University.

## ■ ABBREVIATIONS

spiro-MeOTAD, 2,2',7,7'-tetrakis(*N,N*-di-*p*-methoxyphenylamine)-9,9'-spirobifluorene; HTL, hole transport layer; XPS, X-ray photoelectron spectroscopy; UPS, ultraviolet photoelectron spectroscopy; FTIR, Fourier transform infrared; SEM, scanning electron microscope; AFM, atomic force microscopy; LiTFSI, Li-bis(trifluoromethanesulfonyl)-imide; PCE, power conversion efficiency; DSSCs, dye-sensitized solar cells; *t*-BP, 4-*tert*-butylpyridine;  $J_{sc}$ , short-circuit current;  $V_{oc}$ , open-circuit voltage; MAI, methylammonium iodide; BE, binding energy; *I*–*V*, current–voltage; HOMO, highest occupied molecular orbital;  $\Phi$ , work function; IE, ionization energy; ASF, atomic sensitivity factor

## ■ REFERENCES

- (1) Hagen, J.; Schaffrath, W.; Otschik, P.; Fink, R.; Bacher, A.; Schmidt, H. W.; Haarer, D. *Synth. Met.* **1997**, *89*, 215.
- (2) Bach, U.; Lupo, D.; Comte, P.; Moser, J. E.; Weissortel, F.; Salbeck, J.; Spreitzer, H.; Gratzel, M. *Nature* **1998**, *395*, 583.
- (3) Kim, H. S.; Lee, C. R.; Im, J. H.; Lee, K. B.; Moehl, T.; Marchioro, A.; Moon, S. J.; Humphry-Baker, R.; Yum, J. H.; Moser, J. E.; Gratzel, M.; Park, N. G. *Sci. Rep.* **2012**, *2*, 591.
- (4) Lee, M. M.; Teuscher, J.; Miyasaka, T.; Murakami, T. N.; Snaith, H. J. *Science* **2012**, *338*, 643.
- (5) Liu, M.; Johnston, M. B.; Snaith, H. J. *Nature* **2013**, *501*, 395.
- (6) Burschka, J.; Dualeh, A.; Kessler, F.; Baranoff, E.; Cevey-Ha, N. L.; Yi, C.; Nazeeruddin, M. K.; Gratzel, M. *J. Am. Chem. Soc.* **2011**, *133*, 18042.
- (7) Snaith, H. J.; Moule, A. J.; Klein, C.; Meerholz, K.; Friend, R. H.; Grätzel, M. *Nano Lett.* **2007**, *7*, 3372.
- (8) Dewalque, J.; Colson, P.; Thalluri, G. K. V. V.; Mathis, F.; Chêne, G.; Cloots, R.; Henrist, C. *Org. Electron.* **2014**, *15*, 9.
- (9) Ariga, K.; Yamauchi, Y.; Rydzek, G.; Ji, Q.; Yonamine, Y.; Wu, K. C. W.; Hill, J. P. *Chem. Lett.* **2014**, *43*, 36.
- (10) Krüger, J.; Plass, R.; Cevey, L.; Piccirelli, M.; Grätzel, M.; Bach, U. *Appl. Phys. Lett.* **2001**, *79*, 2085.

- (11) Krüger, J.; Plass, R.; Gratzel, M.; Matthieu, H. J. *Appl. Phys. Lett.* **2002**, *81*, 367.
- (12) Schmidt-Mende, L.; Bach, U.; Humphry-Baker, R.; Horiuchi, T.; Miura, H.; Ito, S.; Uchida, S.; Gratzel, M. *Adv. Mater.* **2005**, *17*, 813.
- (13) Wang, M. K.; Moon, S. J.; Xu, M. F.; Chittibabu, K.; Wang, P.; Cevey-Ha, N. L.; Humphry-Baker, R.; Zakeeruddin, S. M.; Gratzel, M. *Small* **2010**, *6*, 319.
- (14) Cai, N.; Moon, S. J.; Cevey-Ha, L.; Moehl, T.; Humphry-Baker, R.; Wang, P.; Zakeeruddin, S. M.; Gratzel, M. *Nano Lett.* **2011**, *11*, 1452.
- (15) National Renewable Energy Laboratory (NREL). [http://www.nrel.gov/ncpv/images/efficiency\\_chart.jpg](http://www.nrel.gov/ncpv/images/efficiency_chart.jpg).
- (16) Park, N.-G. *J. Phys. Chem. Lett.* **2013**, *4*, 2423.
- (17) Zhou, H.; Chen, Q.; Li, G.; Luo, S.; Song, T.-b.; Duan, H.-S.; Hong, Z.; You, J.; Liu, Y.; Yang, Y. *Science* **2014**, *345*, 542.
- (18) Jeon, N. J.; Noh, J. H.; Kim, Y. C.; Yang, W. S.; Ryu, S.; Il Seol, S. *Nat. Mater.* **2014**, *13*, 897.
- (19) Abate, A.; Leijtens, T.; Pathak, S.; Teuscher, J.; Avolio, R.; Errico, M. E.; Kirkpatrick, J.; Ball, J. M.; Docampo, P.; McPherson, I.; Snaith, H. J. *Phys. Chem. Chem. Phys.* **2013**, *15*, 2572.
- (20) Docampo, P.; Guldin, S.; Leijtens, T.; Noel, N. K.; Steiner, U.; Snaith, H. J. *Adv. Mater.* **2014**, *26*, 4013.
- (21) Ono, L. K.; Schulz, P.; Endres, J. J.; Nikiforov, G. O.; Kato, Y.; Kahn, A.; Qi, Y. *J. Phys. Chem. Lett.* **2014**, *5*, 1374.
- (22) Hock, R.; Mayer, T.; Jaegermann, W. *J. Phys. Chem. C* **2012**, *116*, 18146.
- (23) Ng, T.-W.; Chan, C.-Y.; Yang, Q.-D.; Wei, H.-X.; Lo, M.-F.; Roy, V. A. L.; Zhang, W.-J.; Lee, C.-S. *Org. Electron.* **2013**, *14*, 2743.
- (24) Chen, D. Y.; Tseng, W. H.; Liang, S. P.; Wu, C. I.; Hsu, C. W.; Chi, Y.; Hung, W. Y.; Chou, P. T. *Phys. Chem. Chem. Phys.* **2012**, *14*, 11689.
- (25) Burschka, J.; Kessler, F.; Nazeeruddin, M. K.; Grätzel, M. *Chem. Mater.* **2013**, *25*, 2986.
- (26) Nguyen, W. H.; Bailie, C. D.; Unger, E. L.; McGehee, M. D. *J. Am. Chem. Soc.* **2014**, *136*, 10996.
- (27) Fantacci, S.; De Angelis, F.; Nazeeruddin, M. K.; Grätzel, M. *J. Phys. Chem. C* **2011**, *115*, 23126.
- (28) Cappel, U. B.; Daeneke, T.; Bach, U. *Nano Lett.* **2012**, *12*, 4925.
- (29) Yang, L.; Xu, B.; Bi, D.; Tian, H.; Boschloo, G.; Sun, L.; Hagfeldt, A.; Johansson, E. M. *J. Am. Chem. Soc.* **2013**, *135*, 7378.
- (30) Jorgensen, M.; Norrman, K.; Krebs, F. C. *Sol. Energy Mater. Sol. Cells* **2008**, *92*, 686.
- (31) Dedryvere, R.; Leroy, S.; Martinez, H.; Blanchard, F.; Lemordant, D.; Gonbeau, D. *J. Phys. Chem. B* **2006**, *110*, 12986.
- (32) Gilman, J. B.; Eliason, T. L.; Fast, A.; Vaida, V. *J. Colloid Interface Sci.* **2004**, *280*, 234.
- (33) Schulz, P.; Edri, E.; Kirmayer, S.; Hodes, G.; Cahen, D.; Kahn, A. *Energy Environ. Sci.* **2014**, *7*, 1377.
- (34) Schöllin, R.; Karlsson, M. H.; Eriksson, S. K.; Siegbahn, H.; Johansson, E. M. J.; Rensmo, H. *J. Phys. Chem. C* **2012**, *116*, 26300.
- (35) Linstrom, P. J.; Mallard, W. G., Eds. *NIST Chemistry WebBook*; NIST Standard Reference Database Number 69; National Institute of Standards and Technology: Gaithersburg, MD, 2011. <http://webbook.nist.gov>.
- (36) Wang, Z.; Gao, W.; Huang, X.; Mo, Y.; Chen, L. *J. Raman Spectrosc.* **2001**, *32*, 900.
- (37) Scofield, J. H. *J. Electron Spectrosc. Relat. Phenom.* **1976**, *8*, 129.
- (38) Ensling, D.; Stjern Dahl, M.; Nyten, A.; Gustafsson, T.; Thomas, J. O. *J. Mater. Chem.* **2009**, *19*, 82.
- (39) Du, P.; Lu, J.; Lau, K. C.; Luo, X.; Barenjo, J.; Zhang, X.; Ren, Y.; Zhang, Z.; Curtiss, L. A.; Sun, Y. K.; Amine, K. *Phys. Chem. Chem. Phys.* **2013**, *15*, 5572.
- (40) Tak, Y.; Park, D.; Yong, K. *J. Vac. Sci. Technol., B* **2006**, *24*, 2047.
- (41) Tanaka, K.; Miyahara, K.; Toyoshima, I. *J. Phys. Chem.* **1984**, *88*, 3504.
- (42) Carley, A. F.; Hawkins, G.; Read, S.; Roberts, M. W. *Top. Catal.* **1999**, *8*, 243.
- (43) Calvert, P. *Chem. Mater.* **2001**, *13*, 3299.
- (44) Veinot, J. G. C.; Marks, T. J. *Acc. Chem. Res.* **2005**, *38*, 632.

- (45) Jolt Oostra, A.; Blom, P. W. M.; Michels, J. J. *Org. Electron.* **2014**, *15*, 1166.
- (46) Niu, G.; Li, W.; Meng, F.; Wang, L.; Dong, H.; Qiu, Y. *J. Mater. Chem. A* **2014**, *2*, 705.
- (47) Noh, J. H.; Im, S. H.; Heo, J. H.; Mandal, T. N.; Seok, S. I. *Nano Lett.* **2013**, *13*, 1764.